Flow Turbulence Combust (2010) 84:653–667
DOI 10.1007/s10494-010-9247-6

Comparison Between Numerically Simulated and Experimentally Measured Flowfield Quantities Behind a Pulsejet

Tao Geng · Fei Zheng · Andrey V. Kuznetsov · William L. Roberts · Daniel E. Paxson

Received: 27 March 2009 / Accepted: 14 January 2010 / Published online: 12 May 2010

Abstract Pulsed combustion is receiving renewed interest as a potential route to higher performance in air breathing propulsion and ground based power generation systems. Pulsejets offer a simple experimental device with which to study unsteady combustion phenomena and validate simulations. Previous computational fluid dynamics (CFD) simulations focused primarily on pulsejet combustion and exhaust processes. This paper describes a new inlet sub-model which simulates the fluidic and mechanical operation of a valved pulsejet head. The governing equations for this sub-model are described. Sub-model validation is provided through comparisons of simulated and experimentally measured reed valve motion, and time averaged inlet mass flow rate. The updated pulsejet simulation, with the inlet sub-model implemented, is validated through comparison with experimentally measured combustion chamber pressure, inlet mass flow rate, operational frequency, and thrust. Additionally, the simulated pulsejet exhaust flowfield, which is dominated by a starting vortex ring, is compared with particle imaging velocimetry (PIV) measurements on the bases of velocity, vorticity, and vortex location. The results show good agreement between simulated and experimental data. The inlet sub-model is shown to be critical for the successful modeling of pulsejet operation. This sub-model correctly predicts both the inlet mass flow rate and its phase relationship with the combustion chamber pressure. As a result, the predicted pulsejet thrust agrees very well with experimental data.

Keywords Pulsejet · Valve model · Exhaust flow field · Vortex location · Turbulence

T. Geng · F. Zheng · A. V. Kuznetsov (✉) · W. L. Roberts
Department of Mechanical and Aerospace Engineering,
North Carolina State University, Campus Box 7910,
Raleigh, NC 27695-7910, USA
e-mail: avkuznet@eos.ncsu.edu

D. E. Paxson
NASA Glenn Research Center, Cleveland, OH 44135, USA

Nomenclature

A_e	Exit plane area
A_{in}	Inlet cross-sectional area
A_v	Reed valve flow area
A_{v_min}	Minimal reed valve flow area
k_v	Reed valve spring constant
L_{in}	Length of the upstream end of the inlet
m_v	Reed valve mass
$\dot{m}$	Inlet mass flow rate
$\dot{m}_e$	Exit plane mass flow rate
P_{cc}	Combustion chamber pressure
P_{in}	Pressure at the upstream end of the inlet
P_0	Ambient total pressure
P_{up}	Pressure just upstream of the reed valve
V_{e}	Exit plane average velocity
V_{in}	Inlet velocity
V_{v}	Reed valve velocity
x_{v}	Reed valve position
α	Proportionality constant relating open reed valve area to its position
ρ	Density
τ	Thrust

1 Introduction

The pulsejet is of interest both due to the complexity of the fundamentally unsteady, reactive flowfield and due to its potential applications to create low-cost, scalable, high thrust-to-weight ratio propulsion devices [1, 2]. There is also renewed interest in the application of pulsed combustion devices for achieving pressure-gain heat addition in gas turbine systems [3].

Detailed descriptions of the passively-valved, resonant pulsejet operational cycle can be found in the literature [4, 5]; however, it may briefly be described here as follows. Referring to Fig. 1, the cycle may be divided into three phases:

1. Combustion—Reaction of an air and fuel mixture within the combustion chamber commences. The pressure begins to rise as a result of confinement of the flow. The pressure rise causes the inlet valves to close, preventing backflow. The reaction rate accelerates as the pressure and temperature rise; this, in turn, accelerates the pressure and temperature rise.

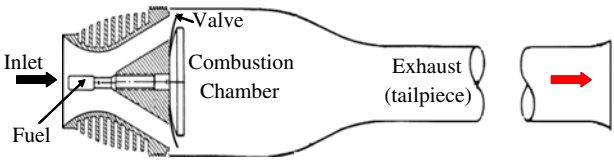

Fig. 1 Pulsejet schematic

2. Expansion—The hot, high-pressure gases in the combustion chamber expand, forcing flow through the exhaust.
3. Ingestion—The momentum of the exhaust gases causes the combustion-chamber pressure to drop below the ambient pressure. This causes the inlet valves to open and a fresh charge of air to enter (mixed with fuel). The residual hot products mix with the fresh charge, initiating a new reaction, and the cycle begins again.

The design and optimization of any pulsed combustion system will rely on accurate flowfield simulations. However, the flowfield, both internal and external, is very complex. For example, the exhaust flow contains a strong starting vortex common to all unsteady, thrust producing flows. The term "starting vortex" originated from studying of a flow around an airfoil, to distinguish from a bound vortex and a trailing vortex; starting vortices have been extensively studied both experimentally and computationally [6–14] in a variety of unsteady devices. However, in most of cited work, the flowfields are not nearly as complex as that of the pulsejet. That is to say, they do not contain comparable turbulence levels, driver and driven enthalpy ratios, vorticity levels, or accelerations. Other challenges include predicting the periodic combustion process, the associated pressure rise in the combustion chamber, and the complex, coupled gas dynamic processes in the tailpiece that result in resonant operation. The inlet mass flow, which is a function of the spring force of the reed valve, the combustion chamber pressure and the upstream flow properties, needs to be modeled precisely to provide appropriate response to the internal flowfield variations between cycles. In other words, simulations should be able to model the self-aspirating phenomena of pulsejets. There have been limited numerical studies of pulsejet flows (e.g. [15–18]), and some experimental flowfield measurements (beyond just thrust) [19]. However, the two have rarely been directly compared, and without such comparisons, or validation efforts, conclusions drawn from the computational work are less certain. Furthermore, in these previous studies no efforts were made to model the valved-pulsejet operating in transient mode, which requires a valve model that can dynamically predict the change in inlet mass flow rate based on the flight speed (if not static) and pressure at the valve head. Most of the pulsejet applications, such as for UAV propulsion, do not fly at a constant speed. Without a dynamic valve model, numerical simulations can only provide limited information in the design of these devices. This paper represents a first step toward that end.

Using an experimentally guided, computational fluid dynamic approach, previous work [18–20] established static simulation models and studied the operation of various pulsejet configurations. Numerical simulations were performed utilizing CFX®, a commercially available, 3-D, compressible, viscous, CFD code. In order to capture wave motions and their interactions and to minimize numerical diffusion in the simulations, second-order advection schemes were always used to calculate the advection terms in the discrete finite volume equations. The CFD mesh and time step were optimized to ensure mesh-independent results. These simulations provided physical insights into the pulsejet's operation. Pressure, mean temperature, exit velocity, static thrust, and operational frequency were compared between simulation results and limited experimental data. Although the results showed good agreement in pressure, temperature, exhaust plane velocity, and frequency, simulated total

thrust and inlet mass flow rate were less than those obtained in experiments. This was due to the fact that the pulsejet valve head, which essentially consisted of a short duct and a reed valve, was not fully modeled. Ideally, to fully model the valve head, simulations need to rely on a coupled two-way fluid (gas)–solid (valve) interaction modeling to predict inlet mass flow rate at any valve position. Adding these fluid-structure interactions are well beyond the scope of this paper, and would render an already computationally expensive simulation that much more expensive. Instead the flow through the valve was modeled using an inlet boundary condition [18] that defined the inlet velocity (at standard temperature and pressure) as a linear function of the pressure difference between the ambient pressure and the combustion chamber pressure. This function, based on experimental measurements [18], is given below:

$$V_{in} = \left\{ \begin{array}{c} \dfrac{3\,(P_0 - P_{cc})}{1000} \cdot \dfrac{[m/s]}{[Pa]},\ P_{cc} < P_0 \\ 0,\ P_{cc} > P_0 \end{array} \right\} \tag{1}$$

where P_{cc} is the pressure immediately (5 mm) downstream of the reed valves and P_0 is the ambient pressure. In experiments, air flow rates were measured for various pressure differences across the valve and a function between inlet velocity and pressure difference was derived based on the experimental data, as shown in Eq. 1. Clearly this simple function could not model the inertia effect of the upstream flow in the valve head or the reed valve motion, resulting in a poor prediction of the inlet mass flow rate and its phase relation to the time varying combustion chamber pressure.

The objective of this paper is to simulate the valved pulsejet operation with a full valve model that can accurately predict the inlet mass flow rate by accounting for the inertia effect of the upstream flow and valve motion without resorting to a full fluid-structure interaction algorithm. Similar to the previous work, pressure and velocity data will be compared to experimental data. However, this paper will concentrate on the flowfield at or downstream of the pulsejet exit plane. This is the region where the starting vortex is formed, developed and transformed. This region also arguably represents the most intriguing and challenging region of the flow, and is a good indicator of how well the new dynamic valve model predicts actual valve behavior. Furthermore, the emitted vortex has been strongly tied to the very high levels of entrainment, mixing, and thrust augmentation observed when pulsejets are used in conjunction with ejectors [21–23]. Maximizing this augmentation represents enabling technology for many potential pulsejet-based applications. It is therefore critical to validate the developed simulation code in this flow region.

Furthermore, a detailed set of experimentally measured, velocity related quantities have been obtained in this region and can serve as a set of valuable validation data; particularly since the simulated pulsejet was identical to the one used for the velocity measurements. The experimental data, obtained using particle imaging velocimetry (PIV), were collected in the same manner described in [13] (and will therefore not be presented here). In fact, the same equipment and laboratory setting were used. However, for the [13] measurements, an ejector was present in the exhaust region. For the present work, the ejector was removed.

2 Simulation Model

2.1 Simulation model and grid

Unless specifically stated in this paper, the simulation model shares similar features as those in previous work [18–20]. The simulation is initiated by high-pressure high-temperature products in the combustion chamber exiting the tailpipe. Due to the expansion wave generated at the exit, pressure in the pulsejet combustion chamber drops below ambient pressure. Controlled by the inlet valve model, premixed air-fuel mixture enters the combustion chamber and is ready for the first combustion event. The turbulent flow and premixed propane-air combustion are modeled with the Shear-Stress-Transport (SST) model and Eddy Dissipation Model (EDM), respectively.[1] The combustion model is based on the Westbrook–Dryer single-step propane combustion model [24]. The only reaction products are CO_2 and H_2O. The EDM assumes that reaction is fast compared to turbulent mixing (high Damköhler number), and the reaction rate is proportional to the timescale of turbulent mixing. The timescale of turbulent mixing, which depends on the eddy properties, is proportional to the ratio of turbulence kinetic energy k and turbulence eddy dissipation ε. The $k-\omega$ based SST model is used to give highly accurate predictions of the onset and the amount of flow separation under adverse pressure gradients by the inclusion of transport effects into the eddy-viscosity formulation. The result is a major improvement in terms of predicting flow separation, which is expected to occur in the flared region of the pulsejet tailpiece. The effectiveness of this approach has been demonstrated in a large number of validation studies [25]. The viscous effect in the boundary layer region is modeled by the CFX® automatic near-wall treatment which automatically switches from wall-functions to a low-Reynolds number near wall formulation as the mesh is refined. However, to take advantage of the reduction in errors offered by this low-Reynolds number formulation, at least 10 nodes must be placed in the boundary layer, resulting in a considerable increase in mesh size. A hybrid high quality mesh is created to ensure fine structured hex-mesh in the near wall region and exit plane while relatively coarse unstructured tet-mesh in the remainder of the external flowfield. Figure 2 shows the dimensions of the computational domain used in simulating the pulsejet and external flowfield. These dimensions match those of the experimental device to which the comparison will be made. The model assumes that the flow is 2-D axi-symmetric and only 1/90 (4° in the θ-direction) of the whole domain is modeled. This small 4° angle in θ-direction is used to minimize the error caused by the 2-D assumption while the mesh is in fact a 3-D mesh.

There are total 13,766 elements, of which 362 are tet-meshes. The computations are performed on the North Carolina State IBM Blade center utilizing a single 3.0 GHz Intel Xeon processor. With a 1.0 μs time step, the computation time for one cycle is about 24 h, and typically requires three to five cycles to reach quasi-steady operation.

[1]The experimental pulsejet to which comparison will be made was actually liquid-fueled, with gasoline. However, accurately modeling the complexities of liquid droplet sprays, vaporization, etc. was considered beyond the scope of this work.

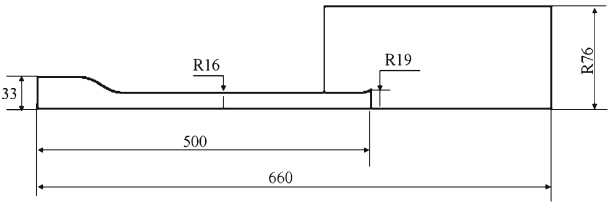

Fig. 2 Dimensions of the simulated pulsejet flowfield (in millimeters)

2.2 Inlet sub-model

The computational simulation includes a modified sub-model of the inlet and reed valve section that is more realistic than previously used [18]. This sub-model is implemented as a boundary condition controlling the total mass flow rate of the premixed reactants into the combustion chamber. As shown in Fig. 3, the mass flow rate is a function of pressure in the valve head and combustion chamber pressure. The valve motion is a function of the spring force and pressure forces acting on both sides of the valve. These two processes are coupled in the sub-model. The inlet flow and reed valve dynamics are modeled by solving three ordinary differential equations that describe their motion:

$$\frac{d\dot{m}}{dt} = \frac{A_{in}}{L_{in}}\left(P_{in} - P_{up}\right) \tag{2}$$

$$\frac{dV_v}{dt} = \frac{\left[A_{in}\left(P_{up} - P_{cc}\right) - k_v x_v\right]}{m_v} \tag{3}$$

$$\frac{dx_v}{dt} = V_v \tag{4}$$

The quantities P_{up}, and A_v are found from the following relations:

$$P_{up} = \begin{cases} P_{cc} + \dfrac{\dot{m}^2}{2\rho}\left(\dfrac{1}{A_v^2} - \dfrac{1}{A_{in}^2}\right), \dot{m} \geq 0 \\ P_{cc} - \dfrac{\dot{m}^2}{2\rho A_v^2}, \dot{m} < 0 \end{cases} \tag{5}$$

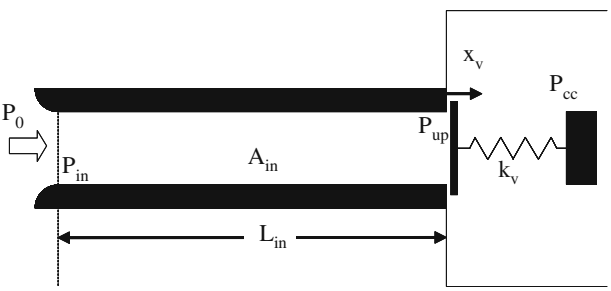

Fig. 3 Valve head model schematic

$$A_v = \max\left(A_{v\_\min}, \alpha x_v\right) \tag{6}$$

Equation 2 describes the mass flow rate and Eqs. 3 and 4 describe the valve motion. The combustion chamber pressure, P_{cc}, is the force function calculated by the code. At each timestep, the sub-model calculates the new mass flow rate based on the current combustion chamber pressure and returns this value to the code, where inlet mass flow rate is specified. Equations 2, 3, and 4 are integrated using a simple, first-order Euler method, with a time step equal to that of the pulsejet simulation. Shown above in Eqs. 5 and 6, the inertia effect of the upstream flow and valve motion are modeled through term P_{up}, the pressure immediately upstream of the valves. Assuming constant density of the reactants in the valve head, P_{up} is calculated from the combustion chamber pressure and mass flow rate in the inlet duct using Bernoulli's equation. The valve open area is calculated in Eq. 6. Because this value is used as denominator in Eq. 5, a minimum value, $A_{v\_\min}$ is set to prevent failure of the equations caused by truncation error when A_v approaching zero. αx_v is the actual valve open area based on the valve location. Before conducting the simulation, an analytical result of the sub-model is obtained to provide a reference for the simulation. This analytical result is obtained by solving Eqs. 2, 3, 4, and 5 with a sinusoidal P_{cc} input using a FORTRAN code.

Figure 4 shows the analytical results of the sub-model response to a sinusoidal variation of the downstream combustion chamber pressure P_{cc} (representing ideal resonant pulsejet operation; actual pressure profiles are not sinusoidal) to verify the response of the sub-model. It is evident that P_{up} and P_{in}, which were assumed to be the same as ambient pressure in previous work [18], are in fact not always equal to ambient pressure. The analytical results also show that the maximum mass flow rate across the valve does not occur at the lowest combustion chamber pressure, as might be expected and implied in the previous work [18]. Instead, it occurs about 0.0005 s after the lowest combustion chamber pressure. Furthermore, Fig. 4b shows that flow into the inlet does not stop when the combustion chamber pressure exceeds the ambient pressure (101,325 Pa). This clearly shows that the inertial effect of the valve and fluid has been successfully predicted by the sub-model. In Fig. 4b, it is evident that valve opens when the combustion chamber pressure is lower than the

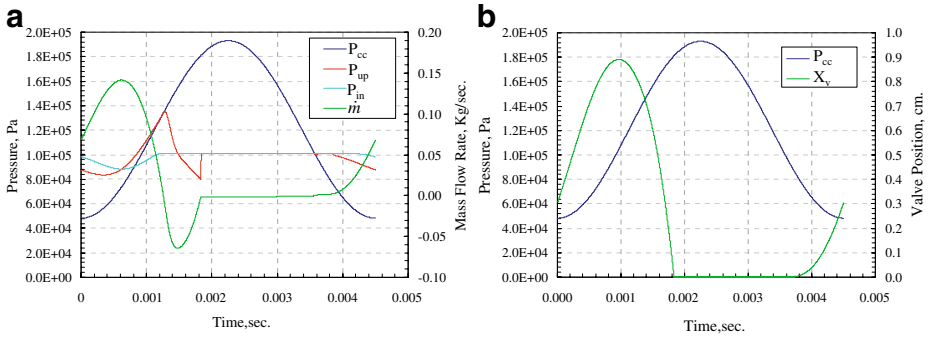

Fig. 4 Analytical results of inlet and valve model cycle responses to a sinusoidal approximation of the pulsejet combustion chamber pressure: **a** upstream pressures and mass flow, **b** reed valve position

ambient pressure, as expected. However, the maximum valve opening does not occur at the lowest combustion chamber pressure, but 0.001 s later, due to the dynamics of the valve.

Figure 5 shows the experimental measurements of combustion chamber pressure and valve position over the course of one cycle. This trace can be compared to Fig. 4b, with the caveat that Fig. 4 is for an ideal, sinusoidal pressure variation. The pressure transducer installation is described in [21]. The valve position is measured using a specially fabricated fiber-optic sensor which is described in Appendix. The sensor is not calibrated, since the design is crude, and high accuracy is not expected. The intention of the measurement is to obtain information on when the valve opens and closes relative to the combustion chamber pressure. The precise position is not particularly important. As such, the position data is shown simply as sensor voltage subtracted from the voltage reading when the valve is in the closed position (sensor voltage drops when the valve opens). The experimental data of Fig. 5 looks quite similar to that of Fig. 4b. In particular, the valve is still open after the combustion chamber pressure exceeds the ambient pressure, and it starts opening process when the combustion chamber pressure drops below ambient. Thus, the valve head sub-model and experimental similarities, while not conclusive, do suggest that the sub-model approach used here is valid.

Figure 6 presents the pulsejet simulation (with the valve head sub-model implemented) of combustion chamber pressure and inlet mass flow rate over the course of one cycle. In the simulation model, negative flow (flow going from the combustion chamber to the valve head) is not allowed due to the numerical instability caused by the negative flow. Comparing Fig. 6 with Fig. 4a, it is evident that the inlet sub-model is correctly implemented. The peak mass flow rate does not occur at the lowest combustion chamber pressure, but rather about 0.5 ms later. From 0.015 to 0.033 s, valves are in open position and remain open about 40% of the total cycle time. This result is close to our previous lab observations [18], which suggest that valves are open for about one third of the total operating cycle. More importantly, the cycle-averaged inlet mass flow rate increases from 14 g/s in previous work [18] to 21 g/s. The experimentally measured mass flow rate is 26 g/s [21], providing further indication that the valve head sub-model is correct. This improvement, increasing the inlet mass flux by 50%, is due solely to the utilization of the inlet sub-model and is critical to the accuracy of the final simulation results because with increased mass

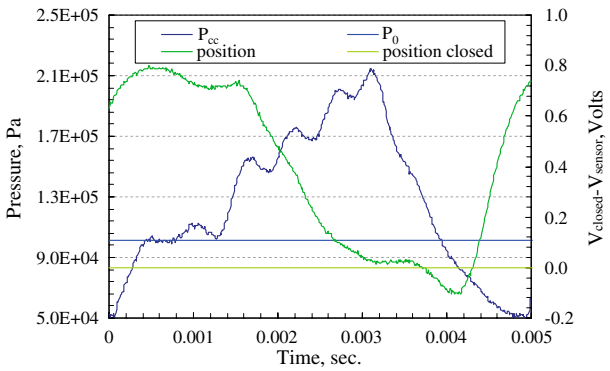

Fig. 5 Measured pulsejet combustion chamber pressure and reed valve position

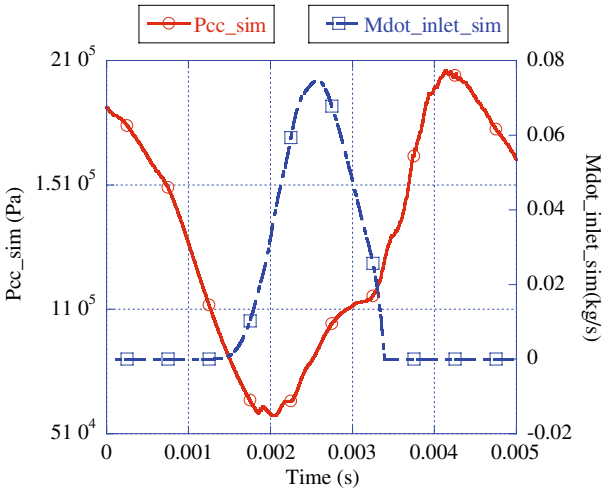

Fig. 6 Simulated pulsejet inlet mass flow rate and combustion chamber pressure

flow rate of reactants, the total thrust increases. This is a desirable effect because previously calculated thrust [18] was smaller than the experimentally measured thrust. Additionally, the correct phase relationship between inlet mass flow rate and combustion chamber pressure is expected to improve predictions of flow dynamics in and out of the pulsejet, which will be evident when examining the exhaust flow.

3 Simulated and Experimental Flow Comparisons and Discussion

As stated in the introduction, the objective of this paper is to validate simulation results by comparing them with experimental data from the pulsejet. Such comparisons are made in this section and include global quantities, such as cycle-averaged thrust and mass flow, as well as time-dependant, local quantities such as combustion chamber pressure and exhaust field velocities.

The experimentally measured thrust is 19.1 N, with a standard deviation of 1.4% [21]. The simulated result is shown in Fig. 7. Thrust is calculated as the integral of the momentum force at the pulsejet exit plane, i.e.:

$$\tau = \int \dot{m}_e V_e dA_e \tag{7}$$

For both the previous [18] and current results, the thrust profiles for three cycles are shown in this figure; cycle-averaged thrusts are computed to be 19.5 and 13.8 N for current and previous results, respectively. Compared to measurements, the error is 1.7% for simulations including the new valve sub-model and 28% for previous result which did not include any valve dynamics. Similar to the pressure, temperature and velocity profiles shown in our previous study [18], Fig. 7 also shows that by adding a dynamic valve/inlet sub-model to the simulation, the model can dynamically and accurately predict the self-aspirating phenomena of pulsejets. Thrust change between two cycles is caused by the change of inlet mass flow rate, which is calculated from upstream flow properties, combustion chamber pressure, and valve spring force in the inlet sub-model.

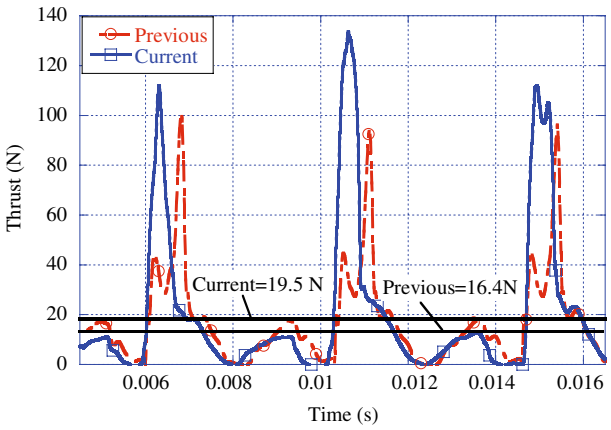

Fig. 7 Simulation results for the pulsejet thrust

Figure 8 shows the simulated and experimentally measured centerline exhaust velocities, at 7 and 210 mm downstream of the pulsejet exit plane, over the course of one cycle. The experimental measurements give the average velocity over an approximately 6 mm span across the centerline, while the simulation results give the exit velocity exactly at the centerline. Combustion chamber pressure (5 mm downstream of the valve) is also included in the plot in order to examine the pressure–velocity phase relationship. Time zero represents the time when combustion chamber pressure reaches its peak value. In the experiments, each PIV contour shown is an ensemble average of 150 phase-locked, instantaneous field measurements. A high frequency transducer monitors cyclic pressure in the pulsejet combustion chamber. When the pressure exceeds a preset threshold value, a phase controlling delay of 300 μs generator is triggered [27]. When the delay is complete, the PIV images are acquired at 125 μs intervals commencing approximately 300 μs after time zero. This 300 μs delay is therefore applied to all the simulation results in this paper. It is evident

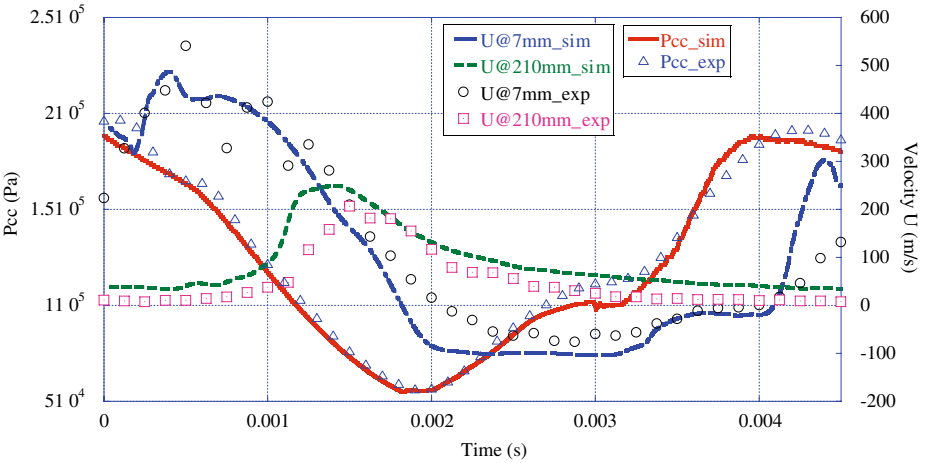

Fig. 8 Phase-locked centerline exhaust velocities

that the simulation agrees very well with measurements in terms of pressure, velocity, and their phase difference. The simulated velocity at 210 mm downstream of the exit is higher than the measured one. This may be caused by the fact that flow velocity diffuses as it travels downstream. Thus, the velocity averaged over several locations around the centerline may be lower than the velocity at the centerline.

Figure 9 compares computed and measured vorticity contours at three different instants during the pulsejet cycle. In each plot, the upper half is the measured PIV

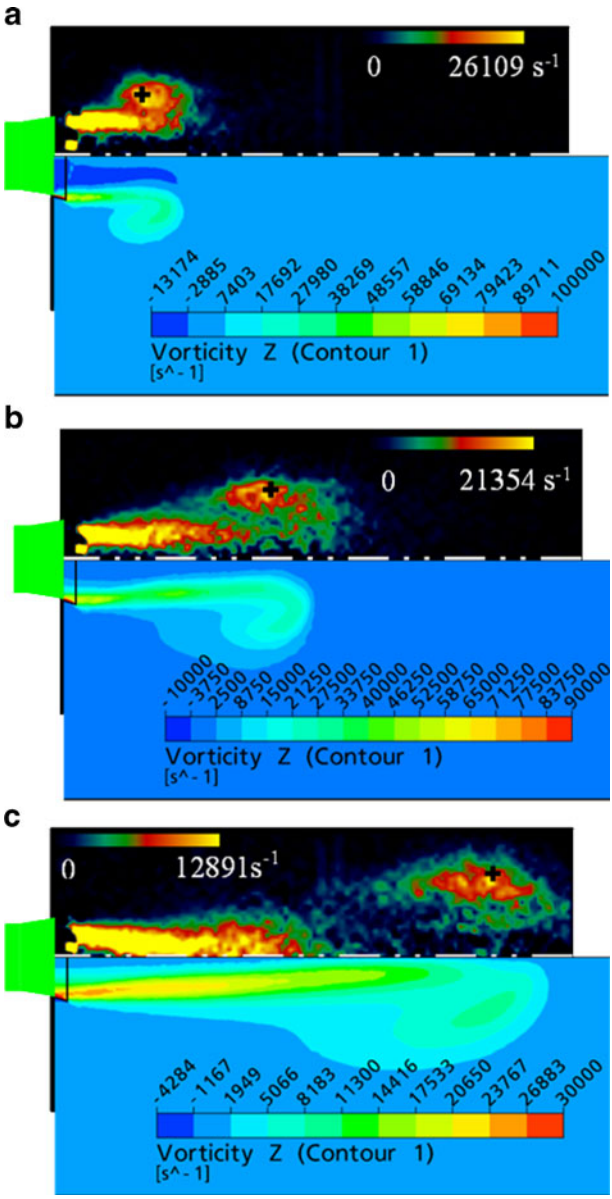

Fig. 9 Experimentally measured and simulated vorticity contours at **a** T = 0.000375 s, **b** T = 0.00075 s and **c** T = 0.0015 s

data and the lower half is the simulated data. The "+" sign in the PIV data represents the location of the highest vorticity value observed in the vortex region. This value, shown on the right hand side of the PIV contour, is used to scale the color spectrum shown, thereby accentuating the vortex. It can be seen from these plots that the simulated vortex has the same convective speed as that measured experimentally. The vorticity levels also agree well between simulation result and experimental data. The highest vorticity location is in the trailing jet area, close to the pulsejet exit plane. Figure 9a shows that the starting vortex ring has just formed from the pulsejet exit shear layer and is still attached to the trailing jet. Possibly owing to this attachment [7, 23], the vortex in Fig. 9a has the highest vorticity value in the vortex core than that in Fig. 9b, c. It is shown in Fig. 9a that negative vorticity appears inside the trailing jet. The negative vorticity is generated by the outer boundary layer of air domain outside the pulsejet [26]. As the vortex travels downstream, it starts to detach from the trailing jet. As a result of this, combined with dissipative forces, the vorticity level of the vortex ring begins to decrease, as shown in Fig. 9b. Later, in Fig. 9c, the vortex is completely detached from the trailing jet, and the vorticity level continues to decrease.

To further verify the simulation results, computational and experimental data on vortex location and combustion chamber pressure are compared in Fig. 10. The location of the vortex is represented by the axial distance from the exit plane to the point in the vortex with the highest vorticity value. From time zero, the vortex locations at each 125 μs interval are compared between simulation and experiment. The comparison shows a good agreement with small but consistent differences after 125 μs. One possible reason for these differences is that after 125 μs, the vortex has traveled near the edge of the simulation domain, where a constant pressure of 101 kPa was specified. This indicates that the simulation domain (external part) may need to be enlarged to minimize the effect of the constant pressure boundary condition. To obtain better simulation results in this area, further investigation is needed to find out the proper external air domain length. This plot also reveals that

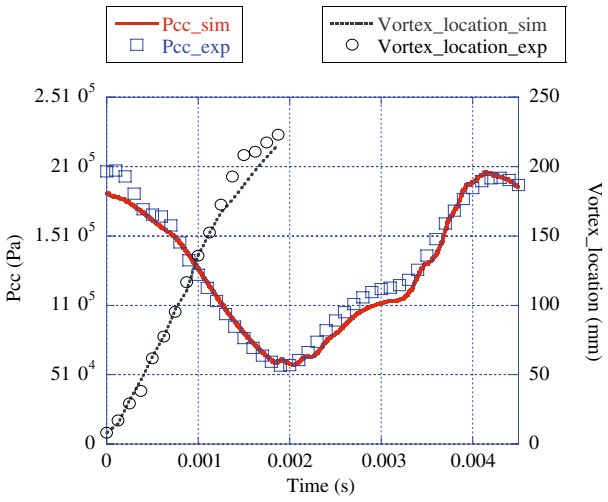

Fig. 10 Measured and simulated vortex location and combustion chamber pressure vs. time

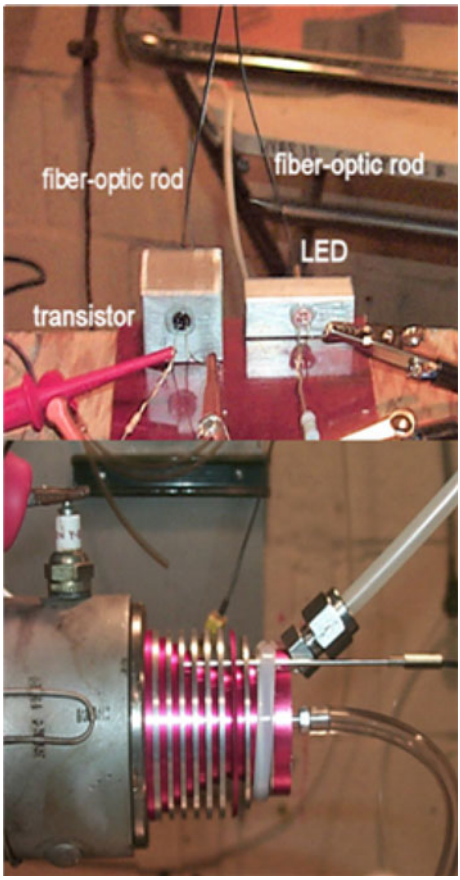

Fig. 11 Optical reed valve position sensor

for the first 150 μs, although the velocity at the centerline changes from about 500 to 200 m/s (Fig. 8), the vortex ring travels at a relatively constant speed of about 135 m/s.

4 Conclusions

This paper provides direct comparisons between experimental measurements and simulation results of a (passively) valved pulsejet. The mathematical model includes a new dynamic inlet sub-model that simulates the valve head dynamics (valve motion and fluid inertia effects) and is integrated into the code. As a result, this new model is able to correctly predict the total thrust and time-averaged mass flow rate, an improvement over the previous model.

In addition to thrust, the simulation model is fully validated by comparisons with experimental data on combustion chamber pressure, exit flow velocity, pressure–velocity phase relationship, vortex ring location and vorticity level. Contrary to expectation, the simulations indicate that the peak inlet mass flow rate occurs about one ninth of a cycle after the minimum in combustion chamber pressure. The inertia effect of the flow inside the valve head plays a key role in the inlet mass flow rate

modeling. Without inertia, the model tends to underpredict the inlet mass flow rate, by as much as 50%.

The comparison of the simulated pulsejet exit flowfield with that measured experimentally also verifies the simulation results. Therefore, the developed dynamic simulation model provides a tool to gain insights into the role of the emitted starting vortex in achieving substantial thrust augmentation and mixing when an ejector is present behind the pulsejet.

Appendix

The optical position sensor constructed for this work is shown installed in the composite photograph of Fig. 11. An infrared LED transmits light down one of the fiber-optic rods shown. This light is emitted from the end of the rod, which is placed in close proximity to the face of the reed valve, in the closed position. The emitted light is therefore reflected from the valve face, and some of it is transmitted through the second fiber optic rod, which terminates into an infrared phototransistor. The light is sufficient to allow the transistor to pass current which, passing also through a resistor, registers a high voltage signal. When the reed valve opens, less of the reflected LED light reaches the transistor, causing the signal voltage to drop.

References

1. Moore, M.: Personal air vehicles: a rural/regional and intra-urban on-demand transportation system. AIAA Pap. 2003–2646 (2003)
2. Skorupa, J.: Military airlift—catching the next wave. AIAA Pap. 2003–2747 (2003)
3. Paxson, D.E.: Ejector enhanced pulsejet based pressure gain combustors: an old idea with a new twist. AIAA Pap. 2005–4216 (2005)
4. Kentfield, J.A.C.: Nonsteady, one-dimensional, internal, compressible flows—theory and applications, vol. 31, pp. 191–235. Oxford University Press, New York (1993)
5. Putnam, A.A., Belles, F.E., Kentfield, J.A.C.: Pulse combustion. Pror. Energy Combust. Sci. **12**, 43–79 (1986)
6. Maxworthy, T.: Turbulent vortex rings. J. Fluid Mech. **64**, 227–239 (1974)
7. Gharib, M., Rambod, E., Shariff, K.: A universal time scale for vortex ring formation. J. Fluid Mech. **360**, 121–140 (1998)
8. Arakeri, J.H., Das, D., Krothapalli, A., Lourenco, L.: Vortex ring formation at the open end of a shock tube: a particle image velocimetry study. Phys. Fluids **16**, 1008–1019 (2004)
9. Rosenfeld, M., Rambod, E., Gharib, M.: Circulation and formation number of laminar vortex rings. J. Fluid Mech. **376**, 297–318 (1998)
10. James, S., Madnia, C.K.: Direct numerical simulation of a laminar vortex ring. Phys. Fluids **8**, 2400–2414 (1996)
11. Nitsche, M.: Scaling properties of vortex ring formation at a circular tube opening. Phys. Fluids **8**, 1848–1855 (1996)
12. Wilson, J., Wernet, M.P., Paxson, D.E.: Vortex rings generated by a shrouded Hartmann–Sprenger tube. AIAA J. **44**(11), 2706–2719 (2006)
13. Paxson, D.E., Wernet, M.P., John, W.T.: Experimental investigation of unsteady thrust augmentation using a speaker-driven jet. AIAA J. **45**(3), 607–615 (2007)
14. Tamburello, D.A., Amitay, M.: Active control of a free jet using a synthetic jet. AIAA pap. 2005–1274 (2005)
15. Erickson, R., Zinn, B.: Numerical investigation of the effect of energy addition processes on pulsejet performance. AIAA Pap. 2004–1210 (2004)
16. Litke P., Schauer, F., Paxson, D.E.: Assessment of the performance of a pulsejet and comparison with a pulsed-detonation engine. AIAA Pap. 2005–228 (2005)

17. Kentfield, J.A.C., Rehman, A., Cronje, J.: Performance of pressure-gain combustors without moving parts. J. Energy **4**(2), 56–63 (1980)
18. Geng, T., Kiker, A., Ordon, R., Kuznetsov, A.V., Zeng, T.F., Roberts, W.L.: Combined numerical and experimental investigation of a hobby-scale pulsejet. J. Propuls. Power **23**(1), 186–193 (2007)
19. Geng, T., Schoen, M.A., Kuznetsov, A.V., Roberts, W.L.: Combined numerical and experimental investigation of a 15-centimeter valveless pulsejet. Flow Turbul. Combust. **78**, 17–33 (2007)
20. Geng, T., Zheng, F., Kiker, A.P., Kuznetsov, A.V., Roberts, W.L.: Experimental and numerical investigation of an 8-centimeter valveless pulsejet. Exp. Therm. Fluid Sci. **31**, 641–647 (2007)
21. Paxson, D.E., Wilson, J., Dougherty, K.: Unsteady ejector performance: an experimental investigation using a pulsejet driver. AIAA Pap. 2002–3915 (2002)
22. Paxson, D.E., Litke, P.J., Schauer, F.R., Bradley R.P., Hoke, J.L.: Performance assessment of a large scale pulsejet-driven ejector system. AIAA Pap. 2006–1021 (2006)
23. Choutapalli, I., Krophatalli, A., Arakeri, J.H.: An experimental study of an axisymmetric turbulent pulsed air jet. J. Fluid Mech. **631**, 23–63 (2009)
24. Westbrook, C.K., Dryer, F.L.: Simplified reaction mechanisms for the oxidation of hydrocarbon. Combust. Sci. Technol. **27**, 31–43 (1981)
25. Bardina, J.E., Huang, P.G., Coakley, T.J.: Turbulence modeling validation testing and development. NASA Tech. Memo. 110446 (1997)
26. Didden, N.: On the formation of vortex rings: rolling-up and production of circulation. Z. Angew. Math. Phys. **30**, 101–116 (1979)
27. Wentworth, T.J., Paxson, D.E., Wernet, M.P.: Conditionally sampled pulsejet driven ejector flow field using DPIV. AIAA Pap. 2002–3231 (2002)